Supporting Information

Non-covalent conjugates of ionic liquid with antibacterial peptide melittin: An efficient combination against bacterial cell

Juhi Saraswat[a], Farooq Ahmed Wani[a], Khalid Imtiyaz Dar[b], M Moshahid Alam Rizvi[b] and Rajan Patel*[a]

[a]Biophysical Chemistry Laboratory, Centre for Interdisciplinary Research in Basic Sciences, Jamia Millia Islamia, New Delhi-110025, India.

[b]Department of Bioscience, Jamia Millia Islamia, New Delhi-110025, India.

*Corresponding author. Tel.: +91 8860634100; fax: +91 11 26983409.

Email address: rpatel@jmi.ac.in (Dr. R. Patel)

Figure captions:

Figure S1. Shows the 1H NMR spectra of [Pyr C_4 NTf_3^-].

Figure S2. Shows the 13C NMR spectra of [Pyr C_4 NTf_3^-].

Figure S3. Shows the FTIR spectra of [Pyr C_4 NTf_3^-].

Figure S4. Shows the mass spectra of [Pyr C_4 NTf_3^-].

Figure S5. Shows the 1H NMR spectra of [Pyr C_6 NTf_3^-].

Figure S6. Shows the 13C NMR spectra of [Pyr C_6 NTf_3^-].

Figure S7. Shows the FTIR spectra of [Pyr C_6 NTf_3^-].

Figure S8. Shows the 1H NMR spectra of [Pyr C_6 NTf_3^-].

Figure S9. Shows the 1H NMR spectra of [Pyr C_8 NTf_3^-].

Figure S10. Shows the 13C NMR spectra of [Pyr C_8 NTf_3^-].

Figure S11. Shows the FTIR NMR spectra of [Pyr C_8 NTf_3^-].

Figure S12. Shows the mass spectra of [Pyr C_8 NTf_3^-].

Figure S13. Shows the 1H NMR spectra of [Pyr C_{10} NTf_3^-].

Figure S14. Shows the 13C NMR spectra of [Pyr C_0 NTf_3^-].

Figure S15. Shows the FTIR spectra of [Pyr C_{10} NTf_3^-].

Figure S16. Shows the mass spectra of [Pyr C_{10} NTf_3^-].

Figure S17. Shows the 1H NMR spectra of [Pyr C_{12} NTf_3^-].

Figure S18. Shows the 13C NMR spectra of [Pyr C_{10} NTf_3^-].

Figure S19. Shows the FTIR of [Pyr C_{12} NTf_3^-].

Figure S20. Shows the mass spectra of [Pyr C_{12} NTf_3^-].

Figure S21. Surface tension as a function of concentration for (a) [Pyr $C_4NTf_3^-$] (b) [Pyr $C_6NTf_3^-$] (c) [Pyr C_8 NTf_3^-] (d)[Pyr C_{10} NTf_3^-] (e) [Pyr $C_{12}NTf_3^-$] at 298 K.

Figure S22. Fluorescence quenching of pyrene as a function of concentration in presence of (a) [Pyr $C_4NTf_3^-$] (b [Pyr $C_6NTf_3^-$] (c) [Pyr C_8 NTf_3^-] (d)[Pyr C_{10} NTf_3^-] (e) [Pyr $C_{12}NTf_3^-$] at 298 K.

Figure S23. Quotient of vibrational band intensities (I_1/I_3) as a function of concentration for (a) [Pyr $C_4NTf_3^-$] (b) [Pyr $C_6NTf_3^-$] (c) [Pyr C_8 NTf_3^-] (d)[Pyr C_{10} NTf_3^-] (e) [Pyr $C_{12}NTf_3^-$] at 298 K.

Figure S24: (a) Fluorescence emission spectra of MEL (5μM) with different concentrations of [Pyr $C_{12}NTf_3^-$] at 298 K (b) shows the van't Hoff plot of ln K_a vs. 1/T for MEL/[Pyr $C_{12}NTf_3^-$] system.

Figure S25. (a) Absorbance spectra of MEL with different concentrations of [Pyr $C_{12}NTf_3^-$] (b) linear plot between 1/Ao-A vs 1/[Pyr $C_{12}NTf_3^-$] (M) at 298 K.

Table captions:

Table S1: Various surface-active parameters of micellization of [Pyr C_4 NTf_3^-], [Pyr C_6 NTf_3], [Pyr C_8 NTf_3^-], [Pyr C_{10} NTf_3^-] and [Pyr C_{12} NTf_3^-] at 298K.

Table S2: Showing the value of binding energy, ΔG^o (kcalmol^{-1}) obtained from molecular docking.

Table S3: Stern-volmer constant (K_{sv}), Binding constant (K_a), number of binding sites *n* and relative thermodynamic parameters for the [Pyr $C_{12}NTf_3^-$]/MEL system at different temperature and 7.2 pH.

Structural characterisation: ^{1}H, ^{13} C NMR, FT-IR and Mass spectroscopy.

1. 1-Butyl-1-methyl-pyrrolidin-1-ium [Pyr C_4 NTf_3^-]. The product was obtained as a brown oil. ^{1}H NMR (400 MHz, $CDCl_3$) δ 3.53–3.46 (m, 4H), 3.33–3.24 (m, 2H), 3.05 (s, 1H), 2.98 (s, 2H), 2.30–2.17 (m, 4H), 1.76–1.67 (m, 2H), 1.45–1.35 (m, 2H), 1.00 (q, J = 7.3 Hz, 3H). ^{13}C NMR (100 MHz, $CDCl_3$) δ 121.2, 117.9, 64.4, 48.2, 25.7, 25.5, 21.5, 21.4, 19.4, 13.4, 13.2, HRMS (ESI) $[M-H]^+$ Calcd for $[C_9H_{20}N]^+$ 142.2613, found 141.2505.

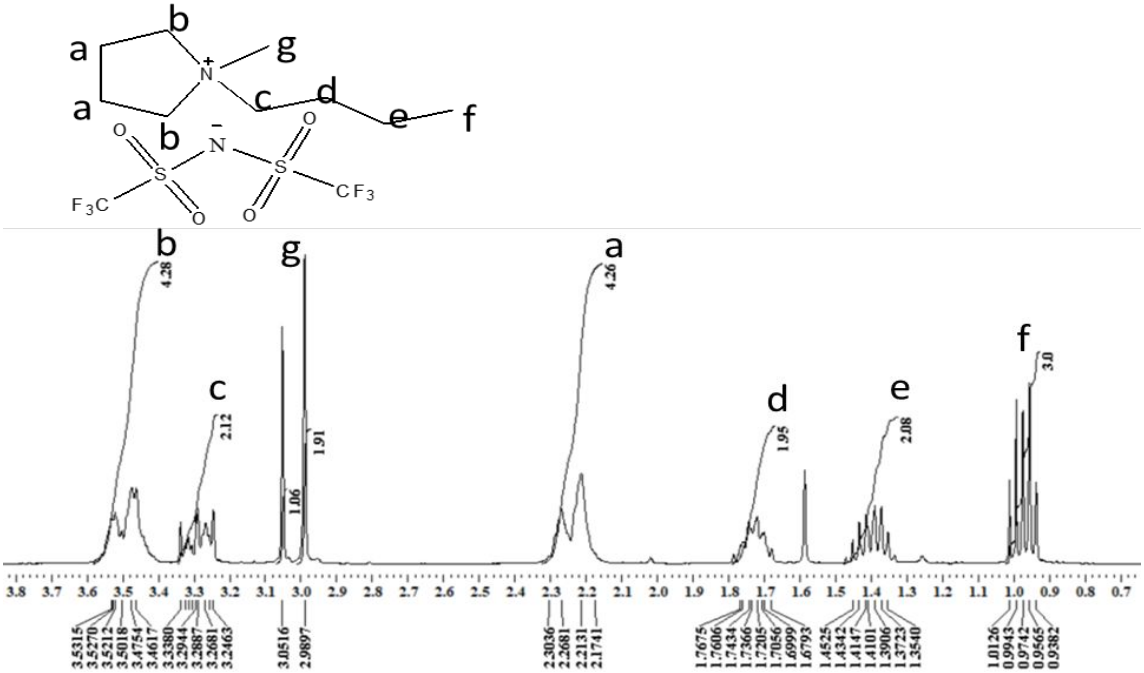

Figure S1. Shows the 1H NMR spectra of [Pyr C_4 NTf_3^-]

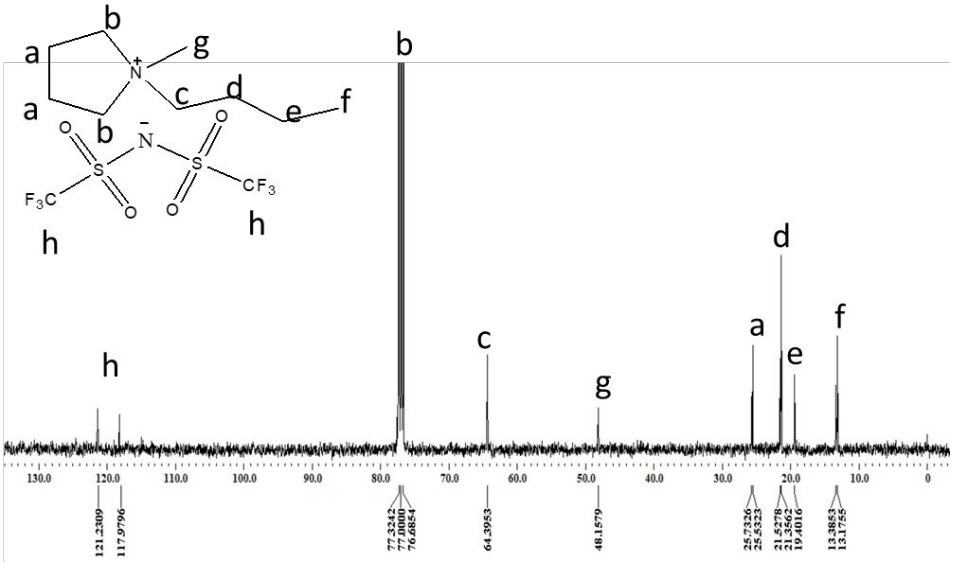

Figure S2. Shows the 13C NMR spectra of [Pyr C_4 NTf_3^-]

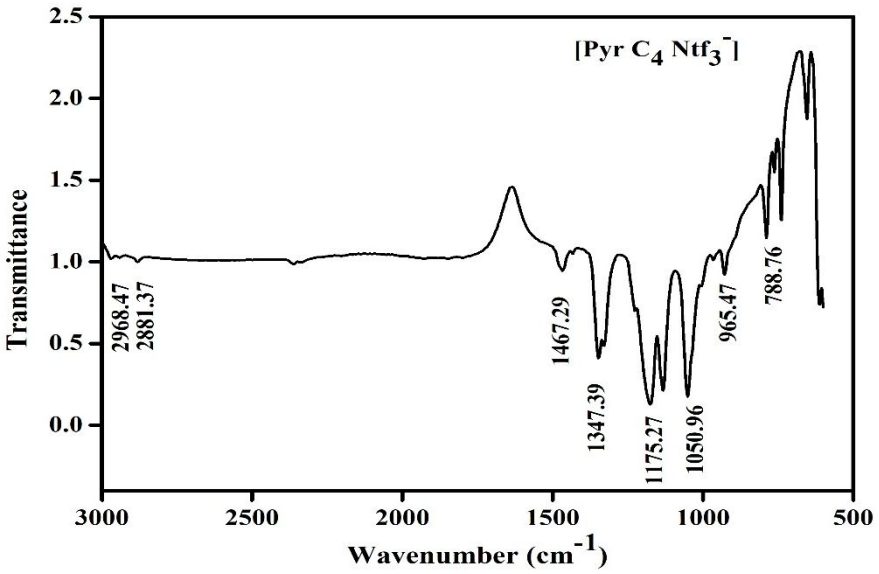

Figure S3. Shows the FTIR spectra of [Pyr C_4 NTf_3^-]

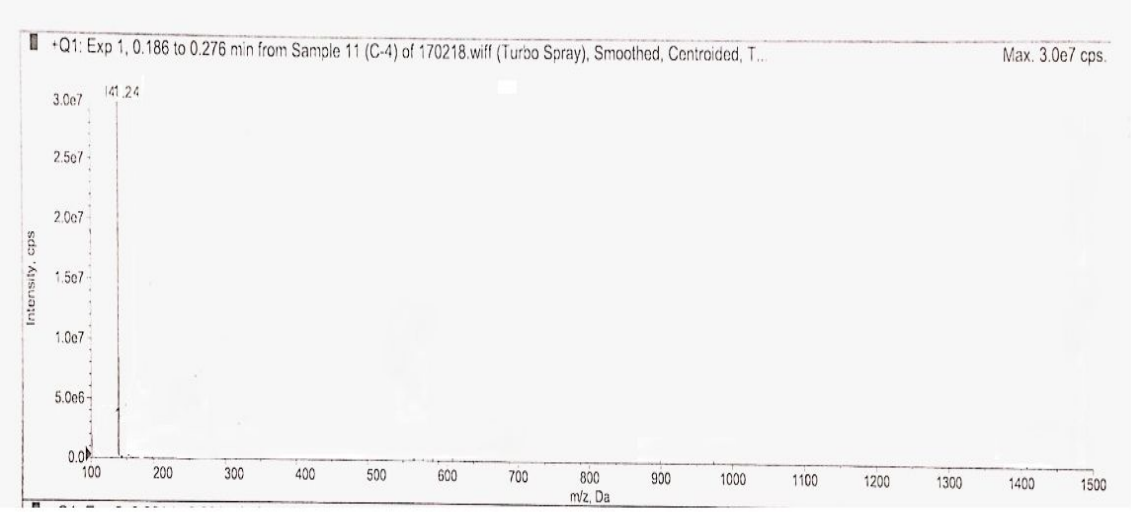

Figure S4. Shows the mass spectra of [Pyr C_4 NTf_3^-]

2. 1-Hexyl-1-methylpyrrolidin-1-ium [Pyr C_6 NTf_3^-]-. The product was obtained as a brown oil. ^{1}H NMR (400 MHz, $CDCl_3$) δ 3.50–3.47 (m, 4H), 3.30–3.26 (m, 2H), 3.02 (s, 3H), 2.26–2.19 (m, 4H), 1.78–1.70 (m, 2H), 1.37–1.30 (m, 6H), 0.89 (t, J = 6.8 Hz, 3H). ^{13}C NMR (100 MHz, $CDCl_3$) δ 121.4, 118.2, 64.7, 64.4, 48.3, 30.9, 25.7, 23.7, 22.2, 21.4, 13.7. HRMS (ESI) $[M+H]^+$ Calcd for $[C_{11}H_{24}N]^+$ 170.314, found 171.325.

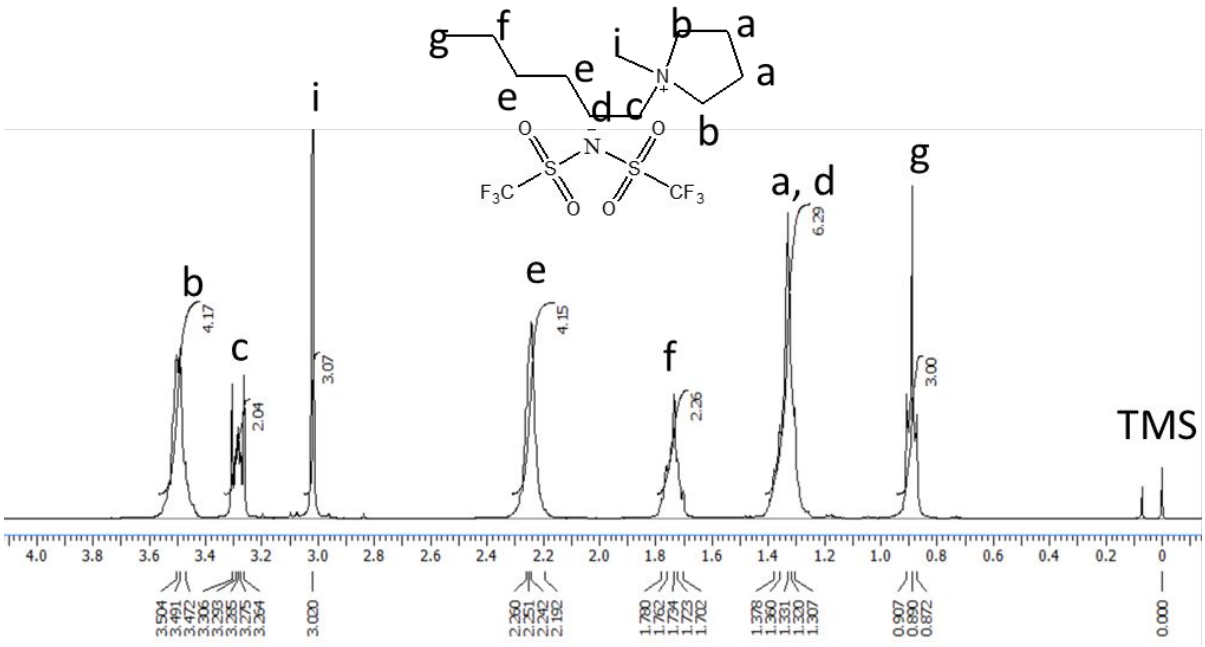

Figure S5. Shows the 1H NMR spectra of [Pyr C_6 NTf_3^-]

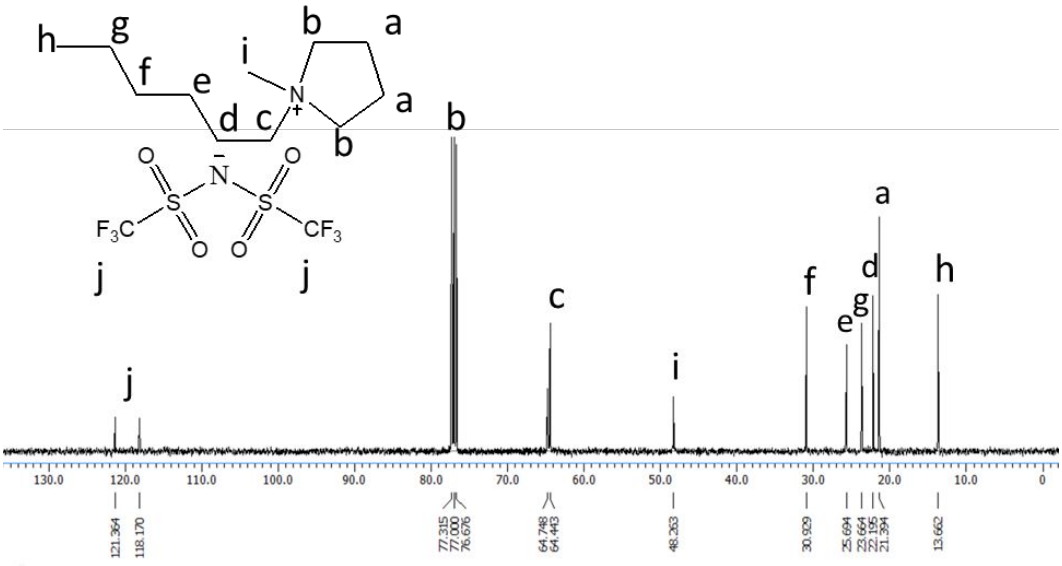

Figure S6. Shows the 13C NMR spectra of [Pyr C_6 NTf_3^-]

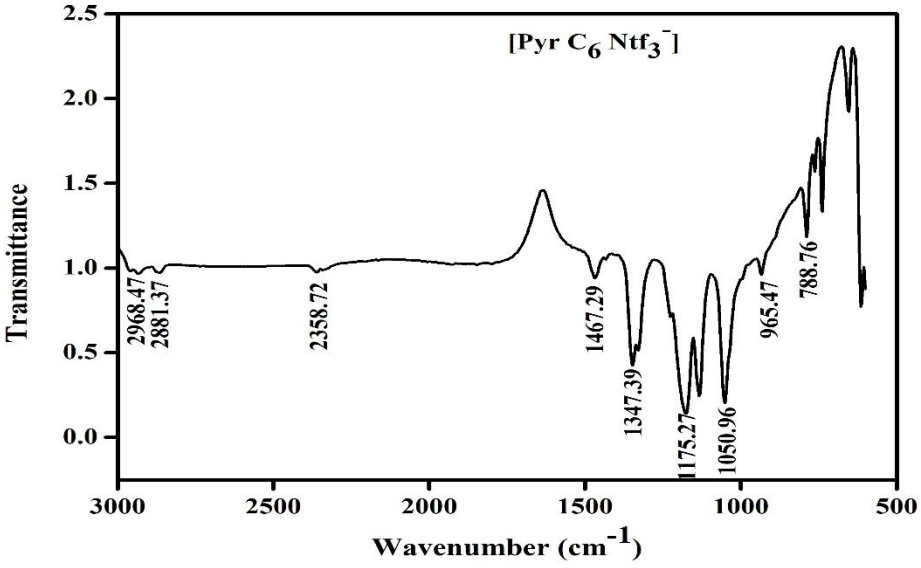

Figure S7. Shows the FTIR spectra of [Pyr C_6 NTf_3^-]

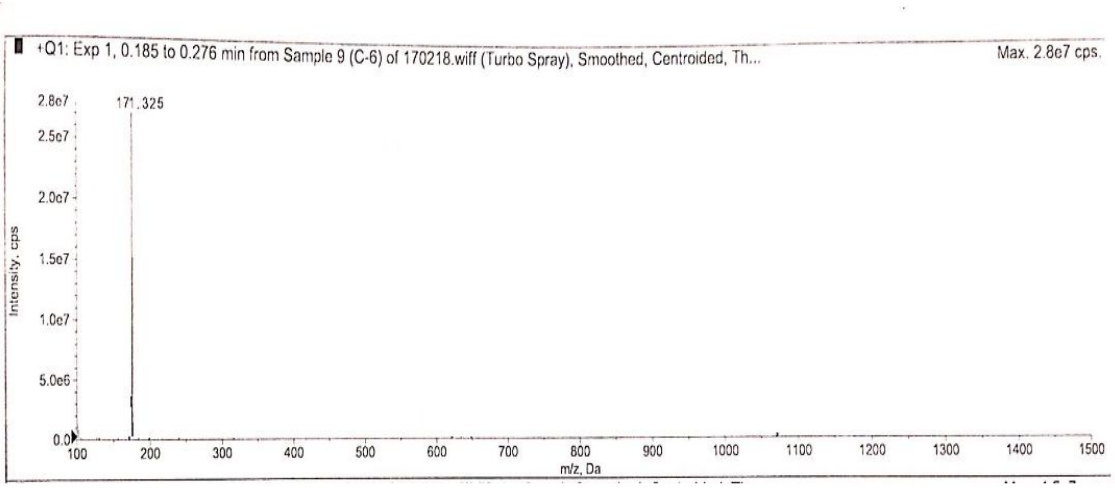

Figure S8. Shows the 1H NMR spectra of [Pyr C_6 NTf_3^-]

3. **1-Methyl-1-octylpyrrolidin-1-ium [Pyr C_8 NTf_3^-].** The product was obtained as a brown oil. ^{1}H NMR (400 MHz, $CDCl_3$) δ 3.50–3.47 (m, 4H), 3.30–3.26 (m, 2H), 3.02 (s, 3H), 2.26–2.19 (m, 4H), 1.78–1.70 (m, 2H), 1.37–1.30 (m, 6H), 0.89 (t, J = 6.8 Hz, 3H). ^{13}C NMR (100 MHz, $CDCl_3$) δ 121.4, 118.2, 64.7, 64.4, 48.3, 30.9, 25.7, 23.7, 22.2, 21.4, 13.7. HRMS (ESI) $[M+Na]^+$ Calcd for $[C_{13}H_{28}N]^+$ 198.3676, found 221.214.

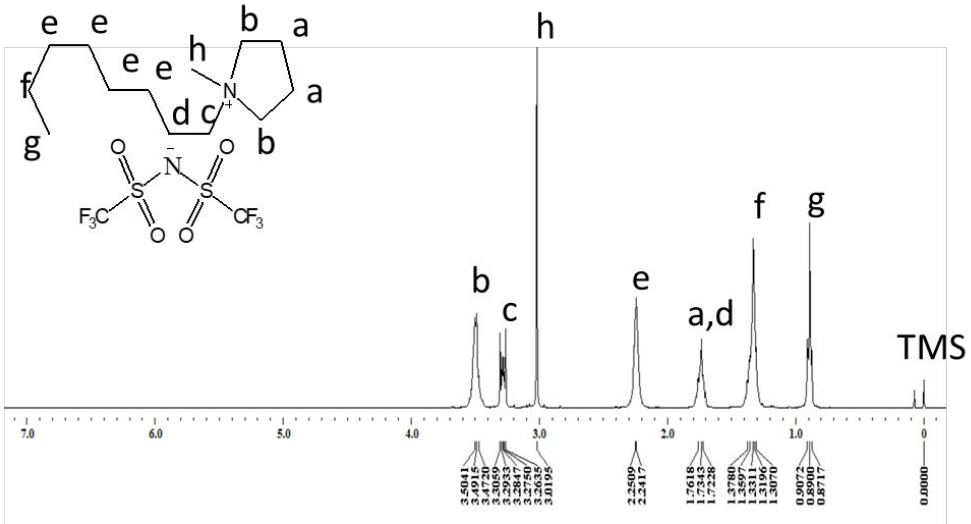

Figure S9. Shows the 1H NMR spectra of [Pyr C_8 NTf_3^-]

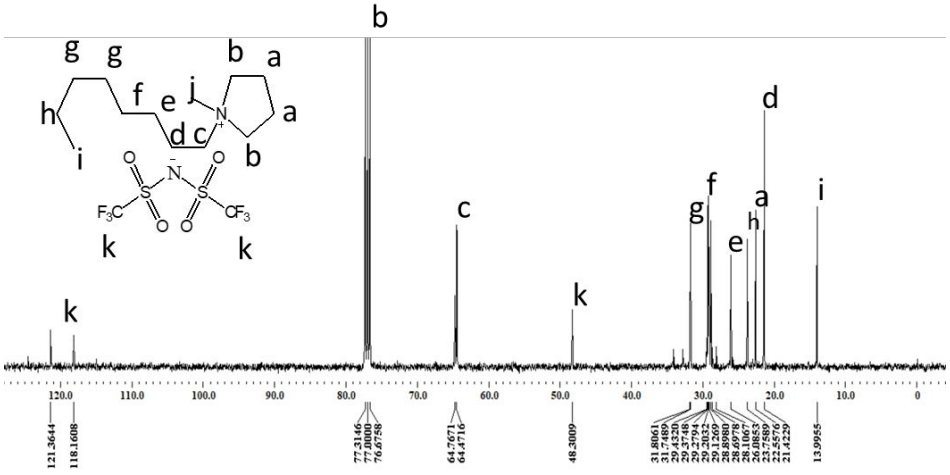

Figure S10. Shows the 13C NMR spectra of [Pyr C_8 NTf_3^-]

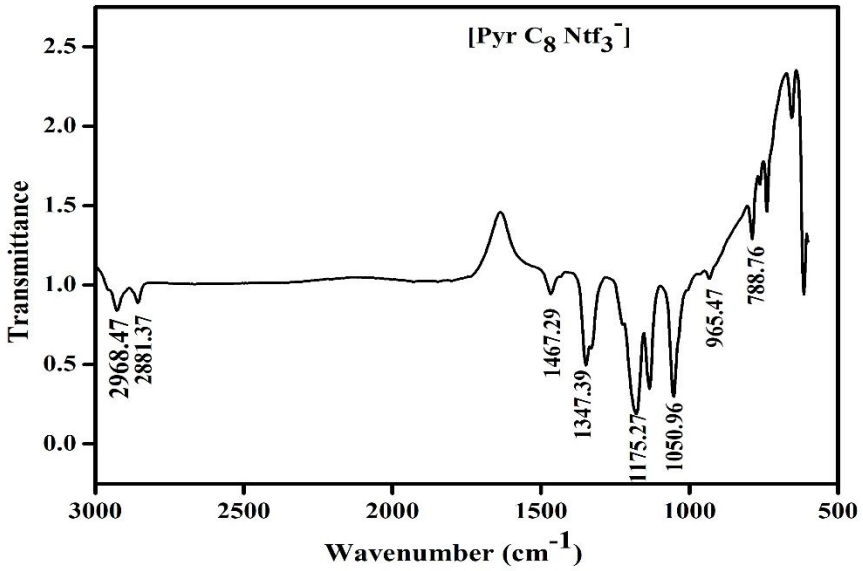

Figure S11. Shows the FTIR NMR spectra of [Pyr C_8 NTf_3^-]

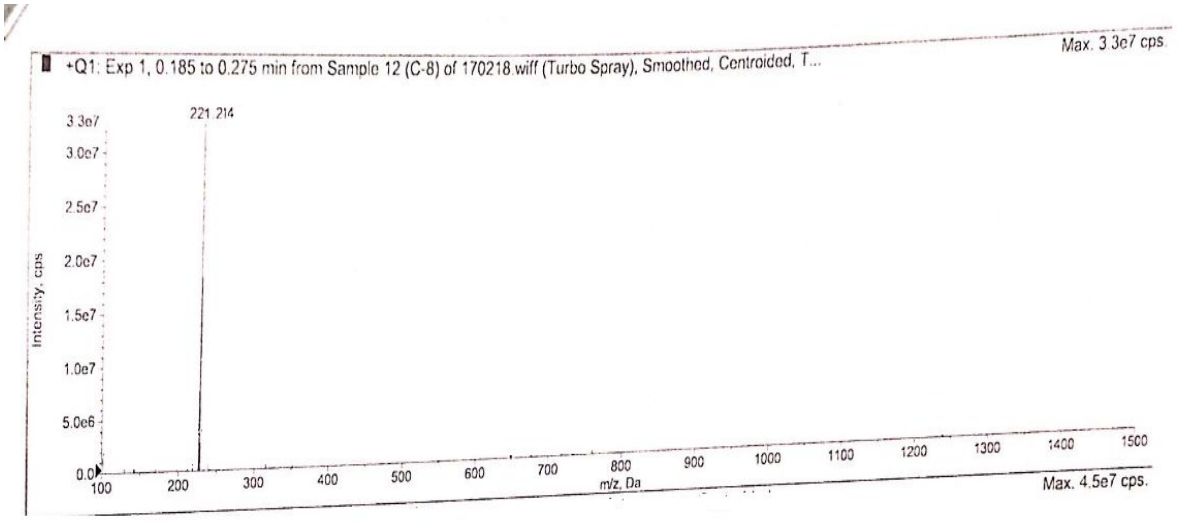

Figure S12. Shows the mass spectra of [Pyr C_8 NTf_3^-]

4. 1-Decyl-1-methylpyrrolidin-1-ium [Pyr C_{10} NTf_3^-]. The product was obtained as a brown oil. ^{1}H NMR (400 MHz, $CDCl_3$) δ 3.48–3.44 (m, 4H), 3.27–3.22 (m, 2H), 2.98 (s, 3H), 2.24–2.16 (m, 4H), 1.72–1.66 (m, 2H), 1.30–1.23 (m, 13H), 0.84 (t, J = 6.4 Hz, 3H). ^{13}C NMR (100 MHz, $CDCl_3$) δ 121.4, 118.2, 64.8, 64.5, 48.3, 34.1, 32.8, 31.8, 29.5, 29.3, 28.9, 28.7, 26.1, 23.8, 22.6, 21.4, 14.0. HRMS (ESI) $[M+H]^+$ Calcd for $[C_{15}H_{32}N^+]$ 226.420, found 227.263.

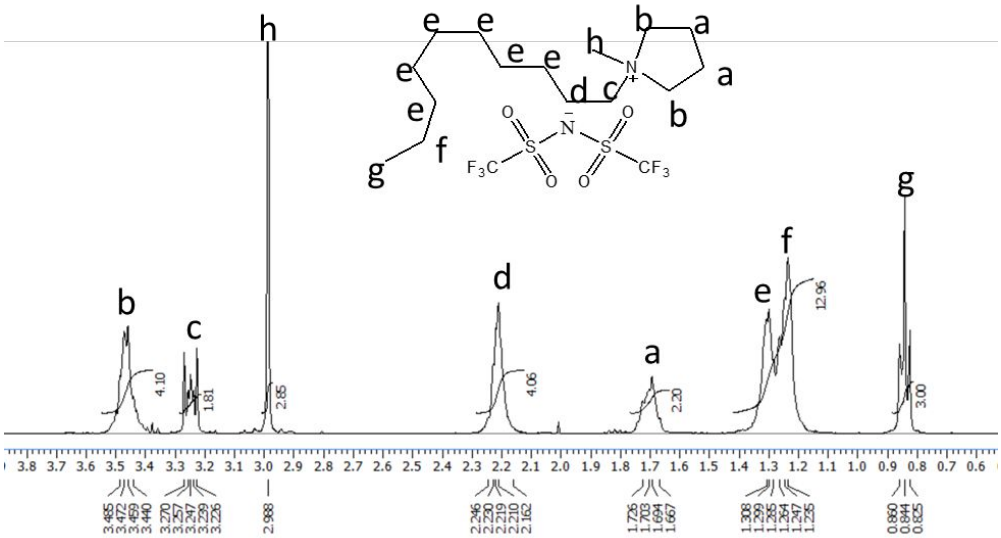

Figure S13. Shows the 1H NMR spectra of [Pyr C_{10} NTf_3^-]

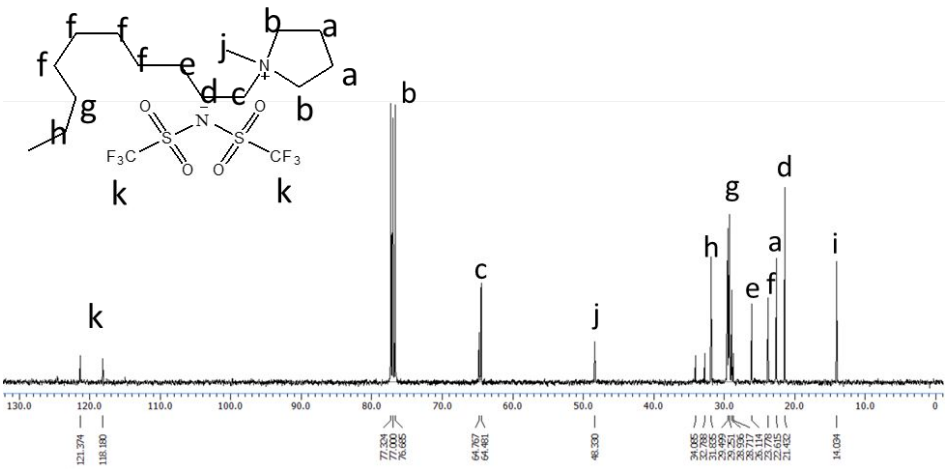

Figure S14. Shows the 13C NMR spectra of [Pyr C_0 NTf_3^-]

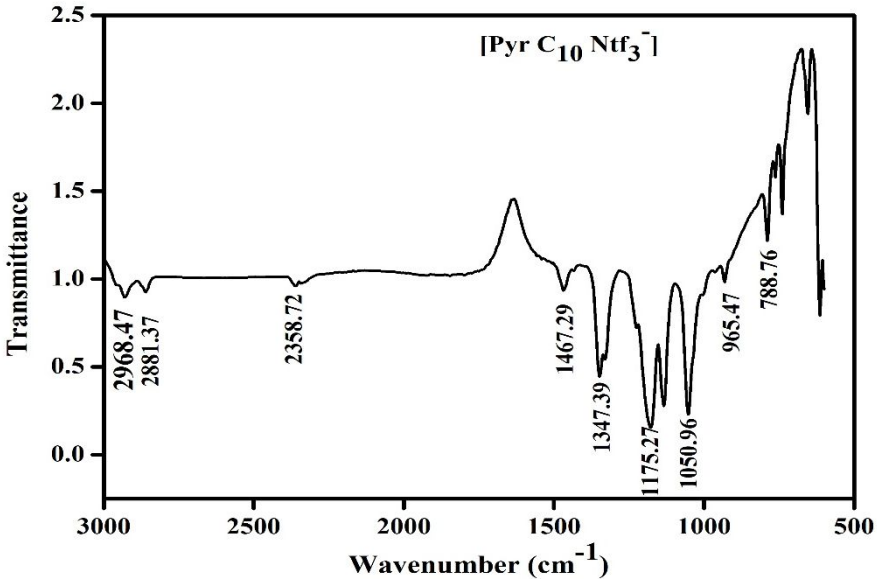

Figure S15. Shows the FTIR spectra of [Pyr C_{10} NTf_3^-]

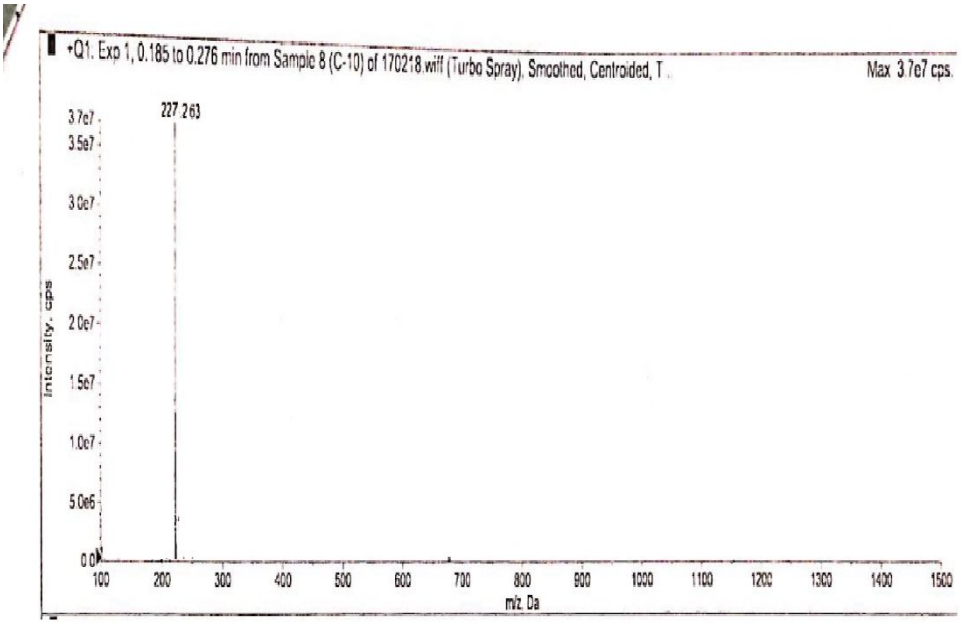

Figure S16. Shows the mass spectra of [Pyr C_{10} NTf_3^-]

5. 1-Dodecyl-1-methylpyrrolidin-1-ium [Pyr C_{12} NTf_3^-]. The product was obtained as a brown oil. ^{1}H NMR (400 MHz, $CDCl_3$) δ 3.52–3.46 (m, 3H), 3.28–3.24 (m, 2H), 3.01 (s, 3H), 2.25–2.23 (m, 3H), 1.75–1.63 (m, 2H), 1.32–1.24 (m, 20H), 0.86 (t, J = 7.2 Hz, 3H). ^{13}C NMR (100 MHz, $CDCl_3$) δ 121.4, 118.2, 64.8, 64.5, 48.2, 31.8, 29.5, 29.4, 29.3, 28.9, 26.1, 23.8, 22.6, 21.4, 14.1, HRMS (ESI) $[M+H]^+$ Calcd for $[C_{17}H_{36}N]^+$ 254.473, found 255.295.

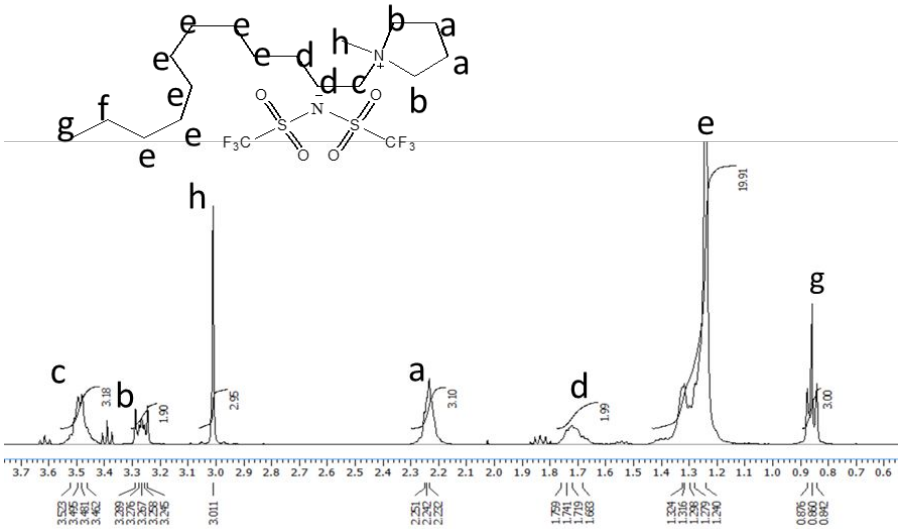

Figure S17. Shows the 1H NMR spectra of [Pyr C_{12} NTf_3^-]

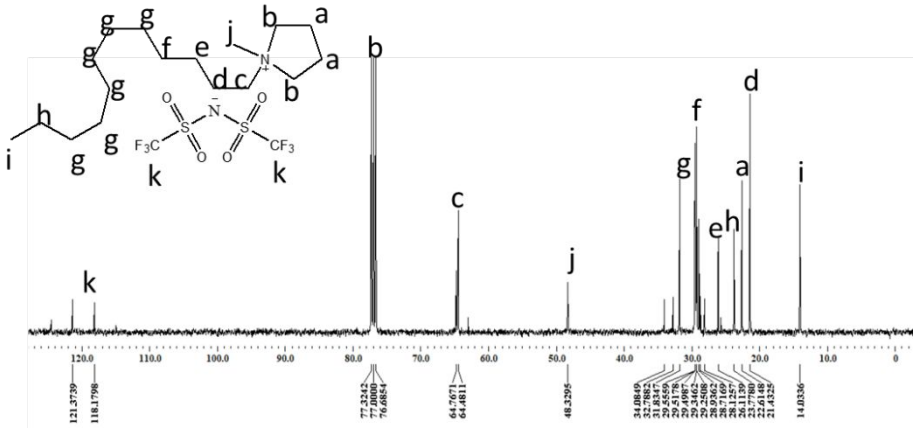

Figure S18. Shows the 13C NMR spectra of [Pyr C_{10} NTf_3^-]

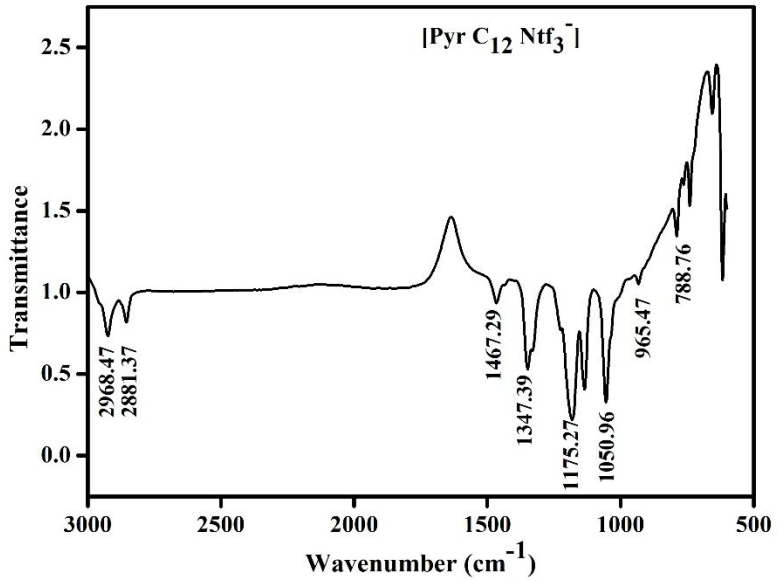

Figure S19. Shows the FTIR of [Pyr C_{12} NTf_3^-]

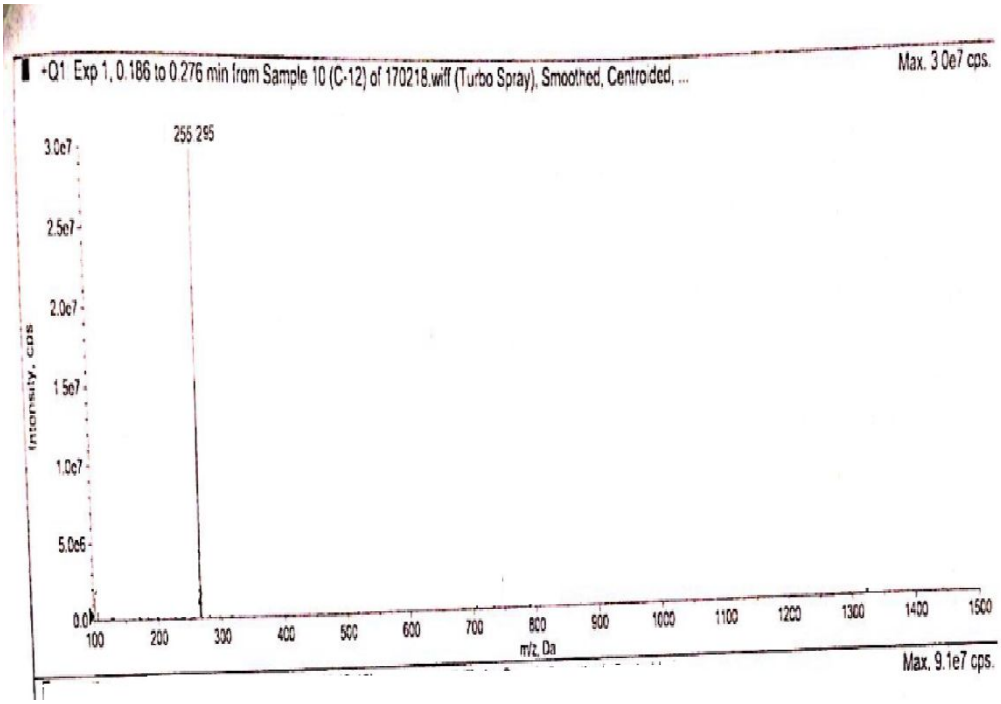

Figure S20. Shows the mass spectra of [Pyr C_{12} NTf_3^-]

Physiochemical characterisation:

Surface Tension Measurement.

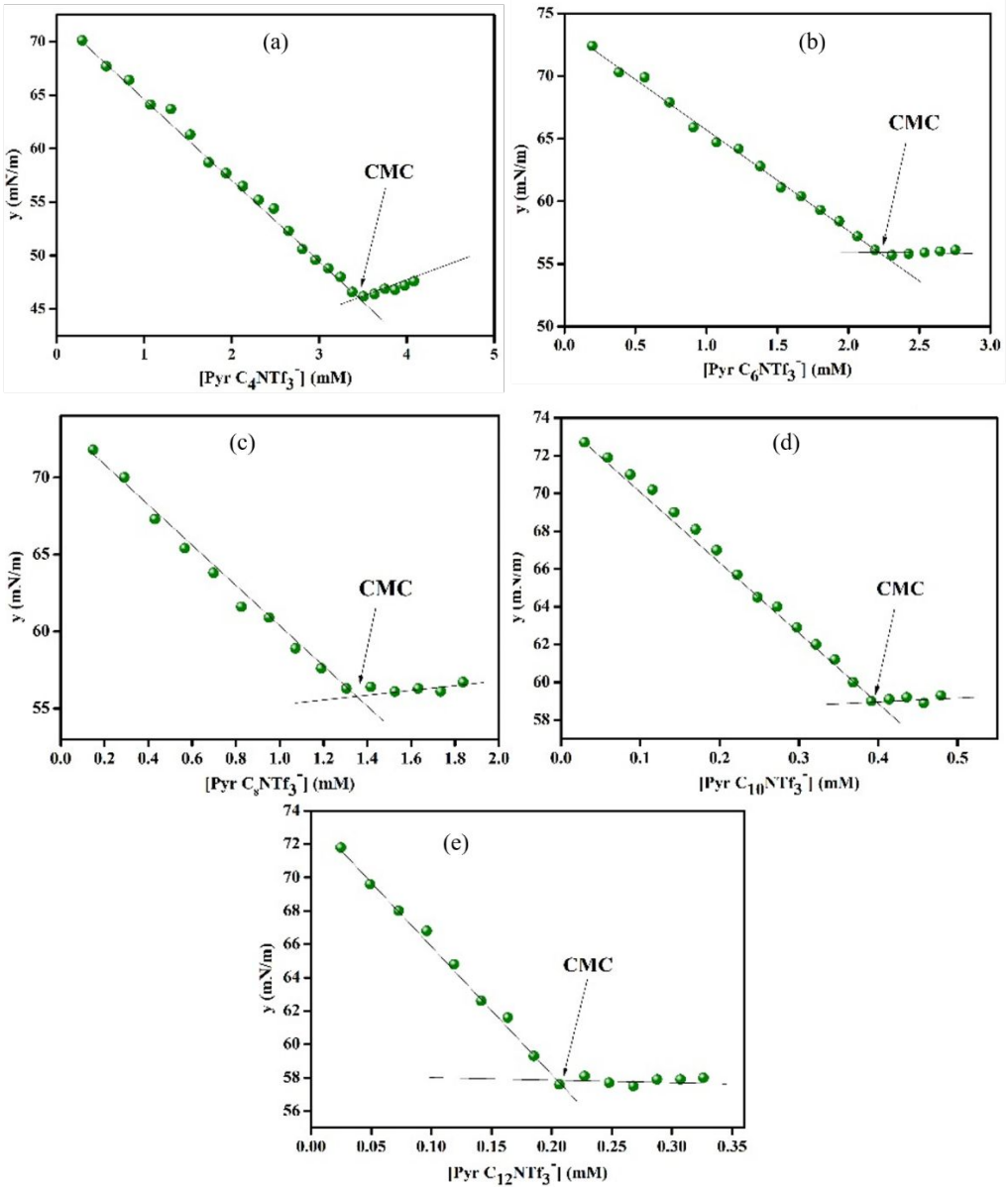

Figure S21. Surface tension as a function of concentration for (a) [Pyr $C_4NTf_3^-$] (b) [Pyr $C_6NTf_3^-$] (c) [Pyr C_8 NTf_3^-] (d)[Pyr C_{10} NTf_3^-] (e) [Pyr $C_{12}NTf_3^-$] at 298 K.

Fluorescence spectroscopy.

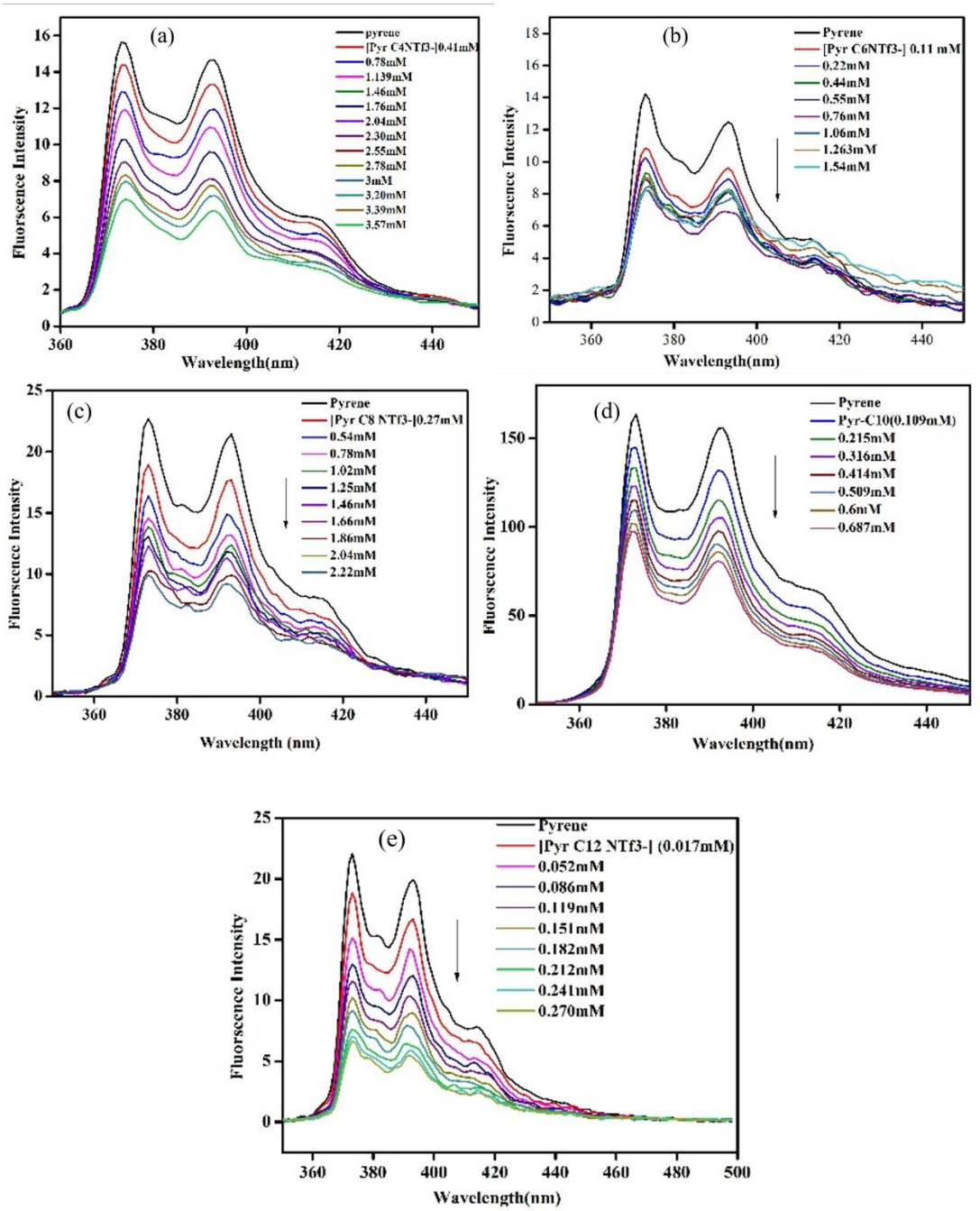

Figure S22. Fluorescence quenching of pyrene as a function of concentration in presence of (a) [Pyr $C_4NTf_3^-$] (b [Pyr $C_6NTf_3^-$] (c) [Pyr C_8 NTf_3^-] (d)[Pyr C_{10} NTf_3^-] (e) [Pyr $C_{12}NTf_3^-$] at 298 K.

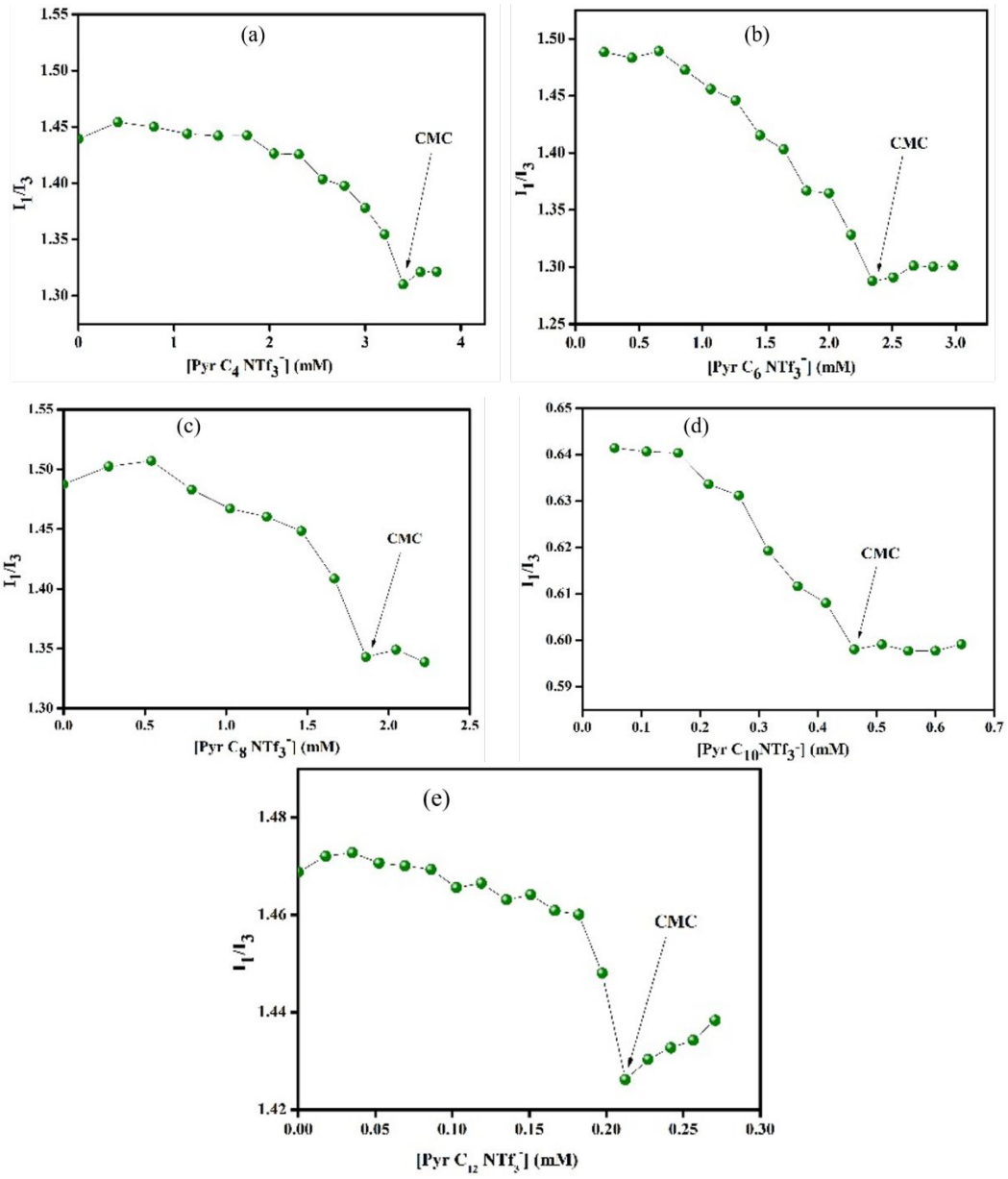

Figure S23. Quotient of vibrational band intensities (I_1/I_3) as a function of concentration for (a) [Pyr $C_4NTf_3^-$] (b) [Pyr $C_6NTf_3^-$] (c) [Pyr C_8 NTf_3^-] (d)[Pyr C_{10} NTf_3^-] (e) [Pyr $C_{12}NTf_3^-$] at 298 K.

Methodology.

Binding Study. The molecular docking study was performed to evaluate the forces involved in the binding process and binding sites of MEL. The docking was done using AutoDock 1.5.6 software. Various docking tools such as the Lamarckian algorithm (LGA), Genetic algorithm based on the local adaptive approach were used to produce the different conformations of the ligand as well as protein [1]. The crystal structure of MEL (PDB ID 1BH1) was obtained from Protein Data Bank (http://www.rscb.org/pdb). Whereas, the structure of ligand was obtained by using ChemDraw (ChemDraw Ultra 8.1), was converted to PDB format by using Open Babel (2.3.0) software and its geometry, as well as energy, was optimized using chem draw. The structure of MEL was assigned Kolmann charges in Autodock [2]. Fifty independent docking runs were carried out for each IL. The results were obtained based on the root mean square (RMSD) criteria. The grid map was calculated for MEL with the AutoGrid tool. After the complete run, according to the binding energy and orientation, the most favourable docking conformation was selected.

Fluorescence measurement was performed to study the conformation change in MEL in the presence of IL if any. The fluorescence spectra of MEL in the absence and presence of [Pyr $C_{12}NTf_3^-$] was recorded on the same instrument as described earlier at 298 K, 303K and 308 K. The excitation and emission slit width was kept 10nm for all the experiments. The temperature was maintained by a constant-temperature cell holder connected to the water circulator (Varian, USA). Fluorescence of MEL (5μM) in Tris buffer (10mM, 7.2 pH) with and without [Pyr $C_{12}NTf_3^-$] (1.66μM to 13.15 μM) where concentration was measured at an excitation wavelength of 280nm and the emission spectra were recorded in a range of 300-450nm [1, 3].

Inner Filter effect. The fluorescence spectra recorded was corrected by using equation 1.

$$Fcorr = Fobsd\ 10^{(A1 + A2)/2} \quad (1)$$

where F_{corr} and F_{obsd} correspond to corrected fluorescence intensities and observed fluorescence intensities, $A1$ and $A2$ are the measured absorbance value at excitation and measured absorbance value at emission wavelength, respectively [4].

The UV-Vis spectra of MEL in the presence and absence of [Pyr $C_{12}NTf_3^-$] was measured at 298 K using the same instrument as described earlier with a wavelength range of 200-400nm. Quartz cuvette of 1cm path length was used for the measurements. Absorbance spectra of MEL were recorded keeping the concentration of constant 10 µM and varied the concentration of [Pyr $C_{12}NTf_3^-$] (from 1.66µM to 13.15 µM) [3, 5].

CD spectra of MEL in presence and absence of [Pyr $C_xNTf_3^-$] were recorded on the same instrument as describes earlier at room temperature, 298 K. The changes in the secondary structure of MEL induces by ILs was monitored in far-UV region (200-250nm) using a quartz cuvette of the path length of 0.1cm [6]. The signal from the reference sample, tris buffer was subtracted from each CD signal of measurements. To improve the signal to noise ratio in CD Spectra measurement, at least 3 accumulation was fixed for every scan. The spectra recorded was converted to the mean residual ellipticity [θ] (deg cm^2 $dmol^{-1}$), which is a concentration-dependent parameter by using relation given below [7].

$$[\theta] = \frac{M_0 \theta_{obsd}}{10LC} \times 10^4 \qquad (2)$$

where θ_{obsd} is observed ellipticity measured in mdeg, M_0 is mean residual weight of the peptide, C is the peptide concentration and l are the path length of the cell in cm. The α-helical content of MEL and MEL with different concentrations of IL can be determined from ellipticity at 222nm (θ_{222} nm/m deg) using equation 3,4 [8].

$$[\alpha](\%) = \frac{100 \times [\theta]_{222}}{\theta_f} \qquad (3)$$

$$\theta_f = -39500 \times \left(1 - \frac{2.54}{n}\right) \qquad (4)$$

where α is the amount of helix and n is the number of amino acid residues, θ_{222} is the observed ellipticity at 222nm. However, the spectra were further used to predict the change in secondary structure dur to the carbon chain length. The ellipticity value at wavelength 222 nm and 207 nm were used to calculate the R-value using the following equation 5 [8-9].

$$R = \frac{[\theta]_{222}}{[\theta]_{222}} \quad (5)$$

where, $[\Theta]_{207}$ and $[\Theta]_{222}$ is the experimentally observed absolute mean residue ellipticity at 207 nm and 222 nm, respectively.

Result and Discussion

Physiochemical characterisation

Surface tension measurement. Surface tension measurements were done to explore the surface-active behaviour of synthesised ILs for which various parameters such as *CMC,* Γ_{max}, A_{min} (listed in Table 1 and Table S1) etc. were determined at room temperature. Figure S21 (a-e) shows the variation of surface tension, γ of synthesized ILs in aqueous medium as a function of their concentration. The surface tension of water was observed to be 72.8 mNm^{-1}, due to the strong interaction between the water molecule, primarily, hydrogen bonding [10]. Progressive decrease in surface tension was observed on addition of IL up to a certain concentration, saturation point is achieved thereafter. After this point, there was no further decrease in surface tension with increasing the concentration of ILs. The breaking point is referred to as critical micellar concentration, CMC. CMC is defined as the concentration of an amphiphile at which micelle formation takes place. The CMC values of synthesised ILs follows the order: [Pyr $C_4NTf_3^-$]>[Pyr C_6 NTf_3^-]>[Pyr $C_8NTf_3^-$]>[Pyr $C_{10}NTf_3^-$]>[Pyr $C_{12}NTf_3^-$]. The values of CMC are listed in Table 1 The values suggest that with increase in alkyl chain length CMC values decrease. The longer alkyl chain length make the ILs more hydrophobic with enhanced surface activity [11] . The obtained CMC values from surface tension were validated by fluorescence spectroscopy discussed in the coming section.

Maximum excess surface area, Γ_{max} and minimum area, A_{min} is the area occupied by single molecule of ILs at air/water interface obtained from Gibb's adsorption isotherm which expresses the compactness of IL molecule over the air/water interface [12]. Smaller the value of Γ_{max} and larger the value of A_{min} depicts the compactness. The value of Γ_{max} can be calculated by using equation 6.

$$\Gamma_{max} = -\frac{1}{2.303nRT}\left(\frac{d\Upsilon}{d\log C}\right) \quad (6)$$

where, γ is the surface tension in mNm^{-1}, R is the universal gas constant (8.314 $Jk^{-1}mol^{-1}$), T is the experimental temperature, C is the concentration of amphiphile, ILs and n is the number of species at the air/water interface after the dissociation of amphiphile. In case of ILs, generally n is taken as 2 because in aqueous medium it dissociates into two parts: cationic and anionic counterpart [10] . Further, to study the packing of molecule at the surface A_{min} was calculated with the help of Γ_{max} by using equation 7.

$$A_{min} = {10^{21}}/{\Gamma_{max} N_A} \quad (7)$$

where, N_A is the Avogadro number (6.023×10^{23}). The calculated values of Γ_{max} and A_{min} are listed in the Table S1. Table S1 shows a continuous decrease in the value of Γ_{max} with increasing chain length whereas, the value of A_{min} has increased. The values show that the molecules at the air/water interface is loosely packed. A_{min} value suggests that as the bulky group increases more repulsive factor comes in to play the value of Γ_{max} for ILs with longer chain length is smaller than that of ILs with smaller alkyl chain length, indicating the decrease in the compactness. Also, the increasing value of A_{min} with increasing chain length suggests the decrease in the packing efficiency at the surface, this might be due to the increased size of the ILs molecule, [Pyr C_{12} NTf_3^-][10, 13].

The pC_{20} parameter was calculated to further investigate the efficiency of interfacial adsorption. The value of pC_{20} parameter is defined as the required concentration of surface-active molecule to reduce the surface tension of water by $20mNm^{-1}$. Greater the value of pC_{20}, greater is the adsorption. Thus, with increase in alkyl chain length the value of pC_{20} slightly has increased which suggests the better adsorption of IL at the surface and further supports the order obtained in the value of Γ_{max} for different ILs. The value of pC_{20} was calculated using equation 8.

$$pC_{20} = -\log C_{20} \quad (8)$$

Surface pressure at CMC (π_{cmc}) was also calculated which depicts the reduction in surface tension at CMC by equation 9.

$$\pi_{cmc} = \Upsilon_o - \Upsilon_{cmc} \quad (9)$$

where, γ_o and γ_{cmc} is the surface tension of pure solvent (water) and surface tension at CMC respectively. The value of π_{cmc} decrease with increasing alkyl chain length corresponding to the effectiveness of ILs to reduce the surface tension. The maximum reduction of CMC was observed in the case of [Pyr C_{12} NTf_3^-], might be due to hydrophobicity.

Further, packing parameters (p) was also calculated by Tanford's formula by using equation 10. The value of p signifies the shape of micelle formed in aqueous medium [14].

$$p = \frac{V_o}{l_c A_{min}} \quad (10)$$

where, V_o is the volume of the hydrophobic group, l_c is the length of the hydrophobic and A_{min} is the minimum area occupied by one molecule at air/water interface. These can be calculated using equation 11, 12.

$$V_o = [0.274 + 0.269(n_c - 1)]\ 2 \quad (11)$$

$$l_c = [0.154 + 0.1265(n_c - 1)] \quad (12)$$

where, n_c is the number of carbon atoms in the hydrocarbon chain length. The value of p listed in Table S1 can be used to analyse the shape of the micelle formed. The values between 0-0.33 predicts the spherical shape of the micelle, 0.33-0.5 cylindrical and 0.5-1 depicts lamellar shape of the micelle [10, 13, 15]. As we can see from the Table S1, the value of p is around 0.8 for [Pyr C4 NTf_3^-] which reflects the lamellar shape of the micelle. However, the value of p decreases upto 0.41 with increasing hydrophobicity which suggests that the lamellar shape of the micelle changes to spherical in case of higher analogs, this may be due to hydrophobic nature of ILs which tends to minimize the surface area. The standard Gibbs free energy of aggregation/micellization, ΔG_m^0 for the ionic solutions is calculated using equation 13.

$$\Delta G_m^o = -RT \ln X_{cmc} \quad (13)$$

The Gibbs free energy of adsorption, ΔG_{ad}^{0} at the interface is the translated form of standard Gibbs free energy calculated by using equation 14.

$$\Delta G_{ad}^{o} = \Delta G_{m}^{o} - \left(\frac{\Pi_{cmc}}{\Gamma_{max}}\right) \quad (14)$$

Fluorescence spectroscopy.

Fluorescence spectroscopy is the versatile technique to investigate the micellar behaviour of various ILs etc. using a probe, pyrene [16] shown in Figure S22 (a-e). It is based on the change in vibrational intensity due to solvent effect. Pyrene being condensed aromatic hydrocarbon shows significant vibrational bands in its fluorescence spectra. The change in the intensity depends on the solvent environment [10b]. The change in fluorescence intensity is observed because of the binding of pyrene with ILs, this provides the convenient method to determine the CMC of ILs. Therefore, in the present study we used pyrene as a probe to evaluate the *CMC* value of synthesised ILs in aqueous medium. Figure S23 (a-e) shows ratio of I_1/I_3 vs concentration [ILs] (mM). The curve was fitted with sigmoidal equation. When reaches at micellar concentration the pyrene moves to hydrophobic environment leading to abrupt decrease in the fluorescence intensity whereas, onset of micellization the change in fluorescence intensity remains unchanged. The breaking point in the plot of I_1/I_3 vs [IL] corresponds to *CMC* value. The *CMC* obtained for ILs using fluorescence spectroscopy also validates the results obtained from surface tension. As the chain length or hydrophobicity of ILs increases, the *CMC* value decreases at 298 K. The value of *CMC* obtained from fluorescence spectroscopy at 298 K are summarised in Table 1.

Binding study.

The quenching of fluorescence intensity is due to the molecular interactions taking such as molecular rearrangement, reactions occurring in the excited state, complex formation in the ground state and also energy transfer mechanism [17]. Commonly, quenching is classified as dynamic and static based on interaction taking place either in excited or in ground state. Static

quenching is due to collision taking place between quencher and fluorophore whereas, dynamic quenching takes place when there is a complex formation between fluorophore and quencher in the ground state. In contrast, dynamic quenching mechanism is characterised by the increasing value of Stern-Volmer quenching constant, K_{SV} [18].

The quenching mechanism is evaluated by using Stern Volmer plot (shown in Figure 11 (a)) using Stern-Volmer equation 15.

$$\frac{Fo}{F} = 1 + Ksv\,[Q] \quad , \qquad (15)$$

Here, F_o and F are the fluorescence intensity of MEL in the absence and presence of ILs. K_{sv} is the Stern-Volmer quenching constant, [Q] concentration of ILs.

Binding parameters.

The fluorescence spectra of MEL in absence and presence of different concentration of IL at 298K, 303K and 308 K, [Pyr C_{12} NTf_3^-] is shown in Figure S24(a). The spectra were further used for the calculation of binding constant and number of binding sites. Equations 16 was used to calculate binding constant and binding site.

$$log\,\frac{Fo-F}{F} = log\,K_a + nlog\,[Q] \qquad (16)$$

here, K_a and n are the binding constant and number of binding sites respectively. Figure 11(b) show the plot between $\log\frac{Fo-F}{F}$ vs $\log\,[Q]$. Slope and intercept value obtained by linear fitting the graph which was further used to calculate the value of K_a and n. The calculated values of K_a and n are summarised in the Table S2. The magnitude of K_a indicates the strong interaction of [Pyr C_{12} NTf_3^-] with MEL. The value of n depicts 1:1 binding between of MEL and [Pyr C_{12} NTf_3^-].

The thermodynamic parameters such as the enthalpy change *(*ΔH), and entropy change (ΔS) and free energy change (ΔG*)* were determined by using following equations (17and 18).

$$\ln K = \frac{\Delta H}{RT} + \frac{\Delta S}{R} \quad (17)$$

$$\Delta G = \Delta H - T\Delta S \quad (18)$$

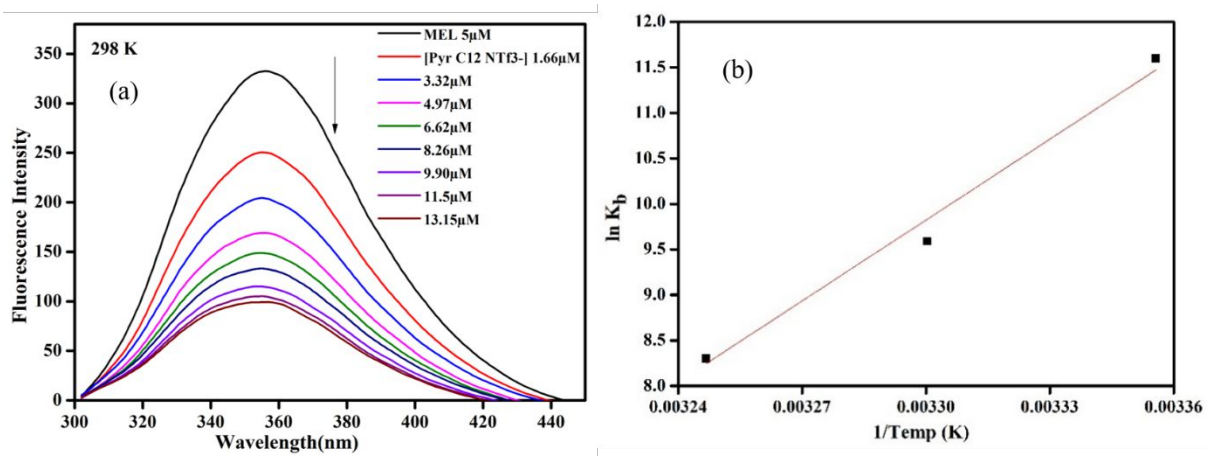

Figure S24: (a) Fluorescence emission spectra of MEL (5μM) with different concentrations of [Pyr $C_{12}NTf_3^-$] at 298 K (b) shows the van't Hoff plot of ln K_a vs. 1/T for MEL/[Pyr $C_{12}NTf_3^-$] system.

UV-Vis Spectroscopy. UV-Vis spectroscopy assists in collecting the insight information regarding structural change and complex formation [19]. The UV-Vis spectrum of MEL in presence and absence of [Pyr C_{12} NTf_3^-] were recorded as shown in (Figure S25 (a)). MEL possessed a peak around 273nm. The prominent absorption spectrum of MEL signifies the presence of tryptophan (chromophore). The UV-Vis spectrum showed an increase in the absorbance of MEL with increasing concentration of [Pyr C_{12} NTf_3][20]. This indicates the complex formation between MEL and [Pyr C_{12} NTf_3]. A reasonable explanation to this observation is the formation of complex in the ground state. In contrast, no change in absorption intensity occurs when it happens on excited state [21]. Binding constant, K_a was also calculated by double reciprocal plot between *1/Ao-A* vs 1/[Pyr C_{12} NTf_3^-] (Figure S25 (b)) using equation 19**,** using the method described earlier [22].

$$\frac{1}{A_o - A} = \frac{1}{A_o} + \frac{1}{KA_o[C]} \quad (19)$$

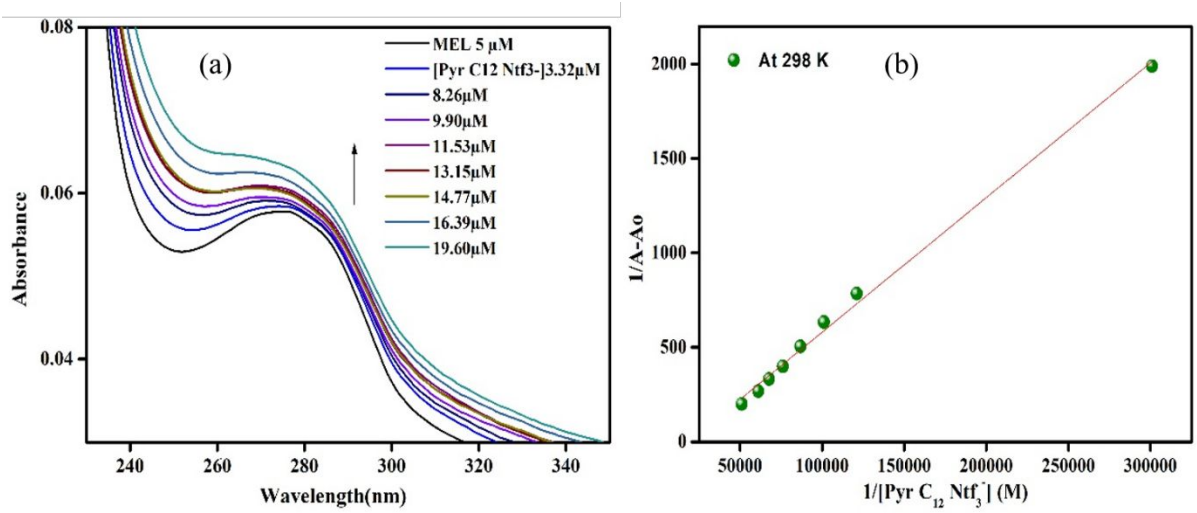

Figure S25. (a) Absorbance spectra of MEL with different concentrations of [Pyr $C_{12}NTf_3^-$] (b) linear plot between 1/Ao-A vs 1/[Pyr $C_{12}NTf_3^-$] (M) at 298 K.

Table S1: Various surface-active parameters of micellization of [Pyr C_4 NTf_3^-], [Pyr C_6 NTf_3^-], [Pyr C_8 NTf_3^-], [Pyr C_{10} NTf_3^-] and [Pyr C_{12} NTf_3^-] at 298K.

S. no.	ILs	Γ_{max} (mol/m^2)×10^{-5}	A_{min} ($Å^2$)	Π_{CMC}	pC_{20}	p
1	[Pyr C_4 NTf_3^-]	3.66	45.29	26.78	1.714	0.894
2	[Pyr C_6 NTf_3^-]	2.38	69.49	17.09	1.714	0.592
3	[Pyr C_8 NTf_3^-]	2.37	69.94	16.98	1.714	0.593
4	[Pyr C_{10} NTf_3^-]	2.20	75.14	13.87	1.720	0.554
5	[Pyr C_{12} NTf_3^-]	1.87	88.66	14.89	1.714	0.471

Table S2: Showing the value of binding energy, ΔG^o (kcalmol^{-1}) obtained from molecular docking.

S.No.	ILs	ΔG^o (kcalmol^{-1})
1.	[Pyr $C_4NTf_3^-$]	-2.31
2.	[Pyr $C_6NTf_3^-$]	-2.41
3.	[Pyr $C_8NTf_3^-$]	-2.69
4.	[Pyr $C_{10}NTf_3^-$]	-2.77
5.	[Pyr $C_{12}NTf_3^-$]	-2.79

Table S3: Stern-volmer constant (K_{sv}), Binding constant (K_a), number of binding sites *n* and relative thermodynamic parameters for the [Pyr $C_{12}NTf_3^-$]/MEL system at different temperature and 7.2 pH.

Temp (K)	K_{sv} ($Lmol^{-1}s^{-1}$)	n	K_a ($L\ mol^{-1}$)	R^2	ΔH ($kJmol^{-1}$)	ΔS ($Jmol^{-1}K^{-1}$)	ΔG ($kJmol^{-1}$)
298	1.88×10^5	0.95	1.20×10^5	0.996	-246.27	-730.96	-28.96
303	1.44×10^5	0.78	0.12×10^5	0.990			-23.65
308	1.13×10^5	0.72	0.04×10^5	0.995			-21.68

References.

1. Gbaj, A. M., Differentiation between Natural and Commercial bee venoms using Fluorescence Spectroscopy. *Pharmacol. Toxicol.* **2018,** *1(2),* 634-642.
2. Mir, M. U. H.; Maurya, J. K.; Ali, S.; Ubaid-Ullah, S.; Khan, A. B.; Patel, R., Molecular interaction of cationic gemini surfactant with bovine serum albumin: A spectroscopic and molecular docking study. *Process Biochem.* **2014,** *49 (4)*, 623-630.
3. Patel, R.; Mir, M. U. H.; Maurya, J. K.; Singh, U. K.; Maurya, N.; Parray, M. u. d.; Khan, A. B.; Ali, A., Spectroscopic and molecular modelling analysis of the interaction between ethane-1, 2-diyl bis (N, N-dimethyl-N-hexadecylammoniumacetoxy) dichloride and bovine serum albumin. *Luminescence* **2015,** *30* (8), 1233-1241.
4. Patel, R.; Kumari, M.; Dohare, N.; Khan, A.; Singh, P.; Malik, M.; Kumar, A., Interaction between pyrrolidinium based ionic liquid and bovine serum albumin: a spectroscopic and molecular docking insight. *Biochem Anal Biochem* **2016,** 5 (265), 1-8.
5. Sharma, T.; Dohare, N.; Kumari, M.; Singh, U. K.; Khan, A. B.; Borse, M. S.; Patel, R., Comparative effect of cationic gemini surfactant and its monomeric counterpart on the conformational stability and activity of lysozyme. *RSC Advances* **2017,** *7 (27)*, 16763-16776.
6. Patel, R.; Maurya, N.; Parray, M. u. d.; Farooq, N.; Siddique, A.; Verma, K. L.; Dohare, N., Esterase activity and conformational changes of bovine serum albumin toward interaction with mephedrone: Spectroscopic and computational studies. *J. Mol. Recognit.* **2018**, 1-13.
7. Kumari, M.; Maurya, J. K.; Tasleem, M.; Singh, P.; Patel, R., Probing HSA-ionic liquid interactions by spectroscopic and molecular docking methods. *J. Photoch. Photobio. B.* **2014,** *138*, 27-35.
8. Zhang, S.-K.; Song, J.-w.; Gong, F.; Li, S.-B.; Chang, H.-Y.; Xie, H.-M.; Gao, H.-W.; Tan, Y.-X.; Ji, S.-P., Design of an α-helical antimicrobial peptide with improved cell-selective and potent anti-biofilm activity. *Scientific reports* **2016,** *6*, 27394.
9. Morrisett, J. D.; David, J. S.; Pownall, H. J.; Gotto Jr, A. M., Interaction of an apolipoprotein (apoLP-alanine) with phosphatidylcholine. *Biochemistry* **1973,** *12* (7), 1290-1299.
10. Bhat, A. R.; Wani, F. A.; Alzahrani, K. A.; Alshehri, A. A.; Malik, M. A.; Patel, R., Effect of rifampicin on the interfacial properties of imidazolium ionic liquids and its solubility therein. *J. Mol. Liq.* **2019**, 111347-111386.
11. Mohajeri, E.; Noudeh, G. D., Effect of temperature on the critical micelle concentration and micellization thermodynamic of nonionic surfactants: polyoxyethylene sorbitan fatty acid esters. *J. Chem.* **2012,** *9 (4)*, 2268-2274.
12. Eastoe, J.; Nave, S.; Downer, A.; Paul, A.; Rankin, A.; Tribe, K.; Penfold, J., Adsorption of ionic surfactants at the air− solution interface. *Langmuir* **2000,** *16* (10), 4511-4518.
13. Wani, F. A.; Khan, A. B.; Alshehri, A. A.; Malik, M. A.; Ahmad, R.; Patel, R., Synthesis, characterization and mixed micellization study of benzene sulphonate based gemini surfactant with sodium dodecyl sulphate. *J. Mol. Liq.* **2019,** *285*, 270-278.
14. Tanford, C., Micelle shape and size. *J. Phys. Chem.* **1972,** *76* (21), 3020-3024.
15. Cognigni, A.; Gaertner, P.; Zirbs, R.; Peterlik, H.; Prochazka, K.; Schröder, C.; Bica, K., Surface-active ionic liquids in micellar catalysis: impact of anion selection on reaction rates in nucleophilic substitutions. *Phys. Chem. Chem. Phys.* **2016,** *18* (19), 13375-13384.
16. Behera, K.; Pandey, S., Concentration-dependent dual behavior of hydrophilic ionic liquid in changing properties of aqueous sodium dodecyl sulfate. *J. Phys. Chem. B.* **2007,** *111* (46), 13307-13315.
17. Valeur, B.; Berberan-Santos, M. N., *Molecular fluorescence: principles and applications*. John Wiley & Sons: 2012.

18. Airinei, A.; Tigoianu, R.; Rusu, E.; Dorohoi, D., Fluorescence quenching of anthracene by nitroaromatic compounds. *Dig. J. Nanomater. Biostruct.* **2011,** *6* (3), 1265-1272.
19. Chen, T.; Zhu, S.; Cao, H.; Shang, Y.; Wang, M.; Jiang, G.; Shi, Y.; Lu, T., Studies on the interaction of salvianolic acid B with human hemoglobin by multi-spectroscopic techniques. *Spectrochim. Acta A.* **2011,** *78* (4), 1295-1301.
20. Cheng, Z.-J.; Zhao, H.-M.; Xu, Q.-Y.; Liu, R., Investigation of the interaction between indigotin and two serum albumins by spectroscopic approaches. *J. Pharm. Anal.* **2013,** *3 (4)*, 257-269.
21. Yuan, D.; Shen, Z.; Liu, R.; Gao, C., Study on the interaction of La3+ with bovine serum albumin at molecular level. *J. Lumin.* **2011,** *131* (12), 2478-2482.
22. Zhang, S.; Sun, X.; Qu, F.; Kong, R., Molecular spectroscopic studies on the interaction of ferulic acid with calf thymus DNA. *Spectrochim. Acta A.* **2013,** *112*, 78-83.